ELSEVIER

Remote Sensing of Environment 78 (2001) 83–98

Remote Sensing of Environment

www.elsevier.com/locate/rse

Cloud characterization and clear-sky correction from Landsat-7

R.F. Cahalan[a,*], L. Oreopoulos[a,b], G. Wen[a,b], A. Marshak[a,b], S.-C. Tsay[a], T. DeFelice[c]

[a]*Laboratory for Atmospheres, NASA/Goddard Space Flight Center, Greenbelt, MD 20771, USA*
[b]*Joint Center for Earth Systems Technology, University of Maryland-Baltimore County, 1000 Hilltop Circle, Baltimore, MD 21250, USA*
[c]*Raythean Science Department, SAB, EROS Data Center, Sioux Falls, SD 57198 and NCAR, RAP, Boulder, CO 80307, USA*

Received 10 March 2000; received in revised form 3 January 2001; accepted 30 April 2001

Abstract

Landsat, with its wide swath and high resolution, fills an important mesoscale gap between atmospheric variations seen on a few kilometer scale by local surface instrumentation and the global view of coarser resolution satellites such as MODIS. In this important scale range, Landsat reveals radiative effects on the few hundred-meter scale of common photon mean-free-paths, typical of scattering in clouds at conservative (visible) wavelengths, and even shorter mean-free-paths of absorptive (near-infrared) wavelengths. Landsat also reveals shadowing effects caused by both cloud and vegetation that impact both cloudy and clear-sky radiances. As a result, Landsat has been useful in development of new cloud retrieval methods and new aerosol and surface retrievals that account for photon diffusion and shadowing effects. This paper discusses two new cloud retrieval methods: the nonlocal independent pixel approximation (NIPA) and the normalized difference nadir radiance method (NDNR). We illustrate the improvements in cloud property retrieval enabled by the new low gain settings of Landsat-7 and difficulties found at high gains. Then, we review the recently developed ''path radiance'' method of aerosol retrieval and clear-sky correction using data from the Department of Energy Atmospheric Radiation Measurement (ARM) site in Oklahoma. Nearby clouds change the solar radiation incident on the surface and atmosphere due to indirect illumination from cloud sides. As a result, if clouds are nearby, this extra side-illumination causes clear pixels to appear brighter, which can be mistaken for extra aerosol or higher surface albedo. Thus, cloud properties must be known in order to derive accurate aerosol and surface properties. A three-dimensional (3D) Monte Carlo (MC) radiative transfer simulation illustrates this point and suggests a method to subtract the cloud effect from aerosol and surface retrievals. The main conclusion is that cloud, aerosol, and surface retrievals are linked and must be treated as a combined system. Landsat provides the range of scales necessary to observe the 3D cloud radiative effects that influence joint surface-atmospheric retrievals.

1. Introduction

Images of Earth's surface from Landsat-7 Enhanced Thematic Mapper Plus (ETM+) and other high spatial resolution spaceborne instruments are obscured by aerosols, especially at visible wavelengths, and by clouds at all solar wavelengths. Even that part of the surface not directly underneath cloud is often affected by cloud shadows that diminish the surface illumination or by reflections from cloud sides that enhance the surface illumination. Cloud, aerosol, and surface retrievals are linked and must be treated as a combined system, since the observed at-satellite radiances result from cloud and aerosol scattering and absorption as well as surface reflectance. Sorting these out requires a good atmospheric model that includes realistic aerosol properties and three-dimensional (3D) scattering from nearby clouds. Landsat provides the range of scales necessary to observe 3D cloud and aerosol radiative effects that influence joint surface-atmospheric retrievals.

This paper uses data from the Landsat-7 scenes listed in Table 1 to illustrate recently developed retrieval techniques and to demonstrate the coupled nature of cloud, aerosol, and surface retrievals. These scenes exhibit a variety of latitudes and sun angles, including scenes over land and ocean, and the full range of cloud fraction from entirely overcast subscenes, through partly cloud-scattered cumulus, to subscenes free of any cloud.

1.1. Cloud fractal structure

Cloud optical and physical properties are well known to have fractal scaling behavior over a wide range of length

* Corresponding author. Tel.: +1-301-614-5390.
E-mail address: robert.cahalan@gsfc.nasa.gov (R.F. Cahalan).

0034-4257/01/$ – see front matter
PII: S0034-4257(01)00251-6

Table 1
Short names and information on the Landsat-7 scenes used in this study

Scene	Path, row	Latitude, longitude	Date	SZA
Vortex	6, 83	32.2°S, 81.2°W	9/15/99	48°
TWP	84, 60	0.9°N, 166.1°E	7/15/99	36°
SGP1	28, 35	37.0°N, 99.3°W	6/4/99	24°
SGP2	28, 35	37.0°N, 99.3°W	3/3/00	49°
SGP3	28, 35	37.0°N, 99.3°W	5/6/99	28°

Both TNP and SGP are sites of the Department of Energy's ARM program. The Vortex and SGP1 scenes are shown in Figs. 1 and 9, respectively. SZA Solar Zenity Angle is given in degrees. Latitude and longitude refer to the upper left corner of the scene.

scales (e.g., Cahalan & Snider, 1989). This is illustrated in Fig. 1 by a Landsat-7 image of von Karman vortices shedding from a subtropical Pacific island (DeFelice, Meyer, Xian, & Cahalan, 2000). This vortex street is similar to, but four orders of magnitude larger than, those well known from classical fluid dynamics experiments. Cloud scaling behavior is determined by the scaling properties of the underlying atmospheric flow field. However, scaling properties of cloud radiances are also affected by radiative smoothing and shadowing. Proper removal of these effects in the retrieval of cloud liquid water, and other physical quantities that makes use of the fractal properties, as discussed in Section 2.

The image in Fig. 1 was acquired off the Chilean coast near the Juan Fernandez Islands (also known as the Robinson Crusoe Islands). Information on the scene can be found in the first row of Table 1 and is referred to in this paper as the "vortex scene." The island rises 1640 m into a layer of marine stratocumulus clouds. Such clouds are common in subtropical summer, but this scene shows a rare situation in which an extended steady equatorward wind creates vortex shedding with clockwise flow off the eastern edge and counterclockwise off the western edge of the island. The vortices grow as they advect hundreds of kilometers downwind. Similar vortex streets are created on much smaller scales, for example, in laboratory smoke and soap film experiments (e.g., Batchelor, 1967, Fig. 4.12.6). Observing the same phenomenon extended over a scale 10^4 times larger, as here, dramatizes the fractal nature of atmospheric convection and clouds. (Historical note: The island's namesake, Alejandro Selkirk, on whom "Robinson Crusoe" was based, was stranded there from 1704 to 1710 and survived by catching wild goats with his bare hands and domesticating wild cats to fend off rats that interfered with sleep.) Even in the absence of an island, "zooming in" on stratocumulus clouds like these often reveals vortices and other cloud structures similar to those observed on larger scales. (An example zoom animation, into California marine stratocumulus, is available on the web at http://climate.gsfc.nasa.gov/~cahalan/FractalClouds/Movies/Movies.html.)

The fractal nature of clouds may be used to improve retrievals. A more abstract description of cloud fractal structure is given by wave number spectra of cloud optical properties. These are approximately power laws over a wide range of scales. Deviations from power law behavior reveal length scales of 3D radiation effects (smoothing and shadowing) in clouds. These deviations are used to remove 3D effects, thus improving cloud retrievals, as discussed further in Section 2 below and in Oreopoulos, Marshak, Cahalan, and Wen (2000).

1.2. Independent pixel approximation

Both cloud and clear-sky retrievals typically assume the independent pixel approximation (IPA; see, for example, Cahalan, 1994; Cahalan, Ridgway, Wiscombe, Bell, & Snider, 1994). A given pixel radiance is assumed to depend only on the surface and atmospheric properties of the earth atmosphere column *within that pixel* and not on the surrounding environment. For clear sky, a simple constant point-spread function is sometimes used to account for so-called adjacency effects, but in fact such effects are not constant but depend on sun angle, aerosol loading, surface bidirectional reflectance distribution function (BRDF), and, as we shall show below, properties of nearby clouds.

For overcast clouds, as in Fig. 1, the IPA approach produces large errors in local radiances. But, such errors occur with both signs and tend to average to zero over a sufficiently large horizontal domain, as long as individual pixels in the domain are small enough that within-pixel cloud variability is small. Domain-averaged errors in cloud properties derived from the pixel radiances, such as liquid water and albedo, are also relatively small when compared to "plane-parallel biases" (e.g., see Cahalan, Ridgway, Wiscombe, Harshvardhan, & Gollmer, 1994; Cahalan, Silberstein, & Snider, 1995). For clouds, then, IPA retrievals produce reasonable *average* properties but unrealistic *spatial structure and variability.*

To retrieve cloud *fields* with realistic spatial structure requires methods that account for the mean-free-path and shadowing effects. Such methods must produce retrieved cloud properties independent of solar illumination, surface BRDF, or anything other than the physical properties of clouds (e.g., liquid amount and particle size).

In Section 2, we discuss two cloud optical property retrieval methods that approximately account for 3D smoothing and shadowing effects (Oreopoulos, Cahalan, Marshak, & Wen, 2000): nonlocal IPA (NIPA) and normalized difference nadir reflectivity (NDNR).

In particular, we illustrate the improvements in cloud property retrieval enabled by these methods and the use of the new low gain settings of Landsat-7. We also highlight difficulties found in cloud retrievals from Landsat-7's high gain setting.

1.3. Cloud impact on clear-sky corrections

Similar to cloud retrieval, the use of the IPA in *clear-sky* retrievals can also produce large local errors. In

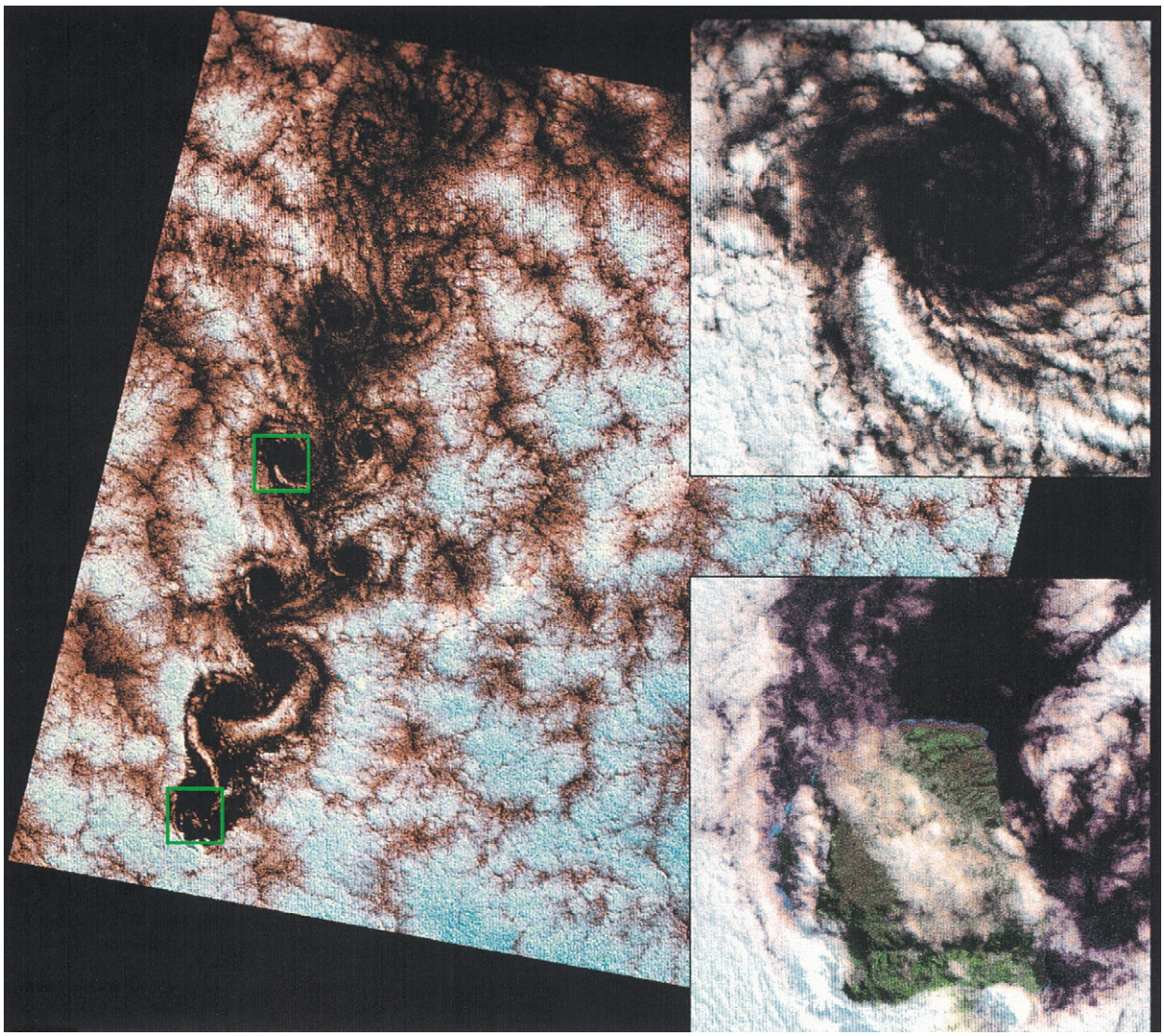

Fig. 1. Landsat-7 image acquired on September 15, 1999 at path 6, row 83, upper left latitude 32.2 south, longitude 81.2 west [full scene 180 km on a side, bands RGB = 742 = (2.2, 0.83, and 0.55) μm]. Taken off the Chilean coast near the Juan Fernandez Islands (also known as the Robinson Crusoe Islands). Alejandro Selkirk Island, in the lower left of the full image, shown zoomed in lower right, rises 1640 m into a layer of marine stratocumulus. Northward from the island is an extended train of von Karman vortices, shedding with clockwise flow off the eastern edge of the island and counterclockwise off the western edge, similar to vortex streets created on much smaller scales in laboratory smoke and soap film experiments. The island's namesake, Alejandro Selkirk, was stranded here from 1704 to 1710. He perhaps noted the leading edge of such vortex streets but could not enjoy the extended view from space or the detail seen in the zoomed view at upper right, seen by Landsat. (See also http://climate.gsfc.nasa.gov/~cahalan/ KarmanVortices.html.)

particular, satellite radiances observed over cloudy and nearby clear sky are not generally independent, so that retrievals of aerosol and surface properties that do not take account of nearby clouds are often inaccurate. That fact is illustrated in this paper with a Landsat ETM+ scene in which one subscene is completely cloud-free while another is partly covered by scattered cumulus. The cumulus increase the illumination of nearby clear pixels, causing an apparent increase in aerosol loading and resulting in inaccuracies in any "clear-sky correction" that ignores cloud effects.

The remainder of this paper is organized as follows. Section 2 summarizes the scales of importance in cloud optical property retrievals, discusses the NIPA and NDNR cloud retrieval techniques, examines the potential for Landsat-7 and surface retrieval comparisons, and illustrates the impact of the new gain settings of Landsat-7 on cloud retrieval. This is followed by Section 3 that reviews the "path radiance" method of aerosol retrieval and clear-sky correction. We also demonstrate in this section the impact of clouds on the aerosol and surface retrievals and interpret this effect using a simplified Monte Carlo (MC) simulation. Section 4 summarizes results, emphasizes the importance of a unified treatment of cloud, aerosol and surface, and stresses the need for testing simple parameterizations.

2. Cloud optical property retrievals

With the recognition in recent years that 3D radiative transfer can have a significant impact on cloud retrievals, the measurements of the TM and ETM+ radiometers are drawing more attention. Because of their high resolution, these instruments are capable of better detecting the effects of 3D cloud structure on reflected solar radiation compared to AVHRR or other lower resolution instruments. Here, we present some of the interrelated aspects of Landsat cloud analysis that form the basis of research on improving cloud optical property retrievals.

2.1. Spectral analysis

Scale breaks (steepening or flattening of log–log slopes), detected in spatial Fourier power spectra of Landsat cloud images, demonstrate the sensitivity of Landsat to radiative processes unresolved by other instruments (Cahalan & Snider, 1989; Marshak, Davis, Wiscombe, & Cahalan, 1995; Oreopoulos, Marshak, et al., 2000). Steepening is observed at small scales (<0.5 km for marine stratus clouds) and is interpreted as a signature of radiative smoothing due to multiple scattering (Marshak et al., 1995). The location of this break is important for obtaining the radiative Green's function, which is used in the IPA extension known as NIPA. In the diffusion regime, the location of the scale break has a known dependence on cloud geometrical and optical thickness (Davis, Marshak, Cahalan, & Wiscombe, 1997; Marshak et al., 1995). Flattening at intermediate and large scales ($>0.5-1$ km) is attributed to side illumination and shadowing effects due to low-order scattering at relatively high solar zenith angles (SZA; Oreopoulos, Marshak, et al., 2000).

Power spectra for ETM+ Bands 4 (B4; 0.83 μm) and 7 (B7; 2.2 μm) of a 1024×1024 pixel overcast subscene taken from the vortex scene are shown in Fig. 2. These illustrate the ability of Landsat-7 to resolve 3D radiative effects. In particular, the spectra show that smoothing prevails at small scales in B4 while roughening dominates at the large and intermediate scales of B7. The wavelength dependence in Fig. 2 is consistent with the anticipated behavior of conservative (B4) vs. absorbing (B7) radiative transfer as seen in MC simulations (see Oreopoulos, Marshak, et al., 2000 for a discussion on single-scattering albedo dependencies). The differences in the spectra are due to the fact that photon path lengths are shorter at absorbing than conservative wavelengths, making radiative smoothing weaker while making the contrast between shadowed and illuminated sides of large cloud cells stronger, which enhances roughening.

The contrasting behavior of 3D radiative transfer at conservative and absorbing wavelengths, revealed by power spectra, can be summarized by plotting least-square-fitted power spectral slopes of one band vs. another. Fig. 3 shows the results of such an analysis using a total of 50 subregions from the Tropical West Pacific (TWP; see Table 1) and the

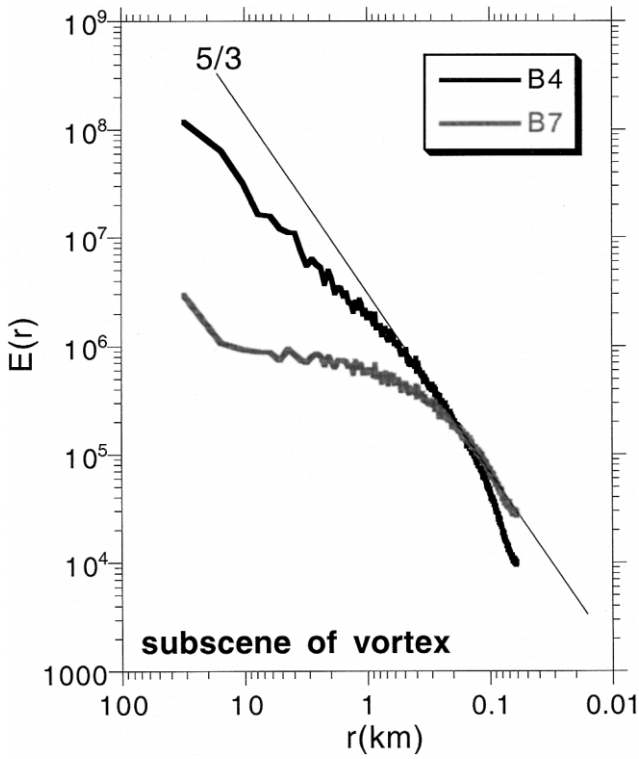

Fig. 2. Average B4 and B7 (0.83 and 2.2 μm) 1D power spectra for 1024×1024 pixel overcast segment of the vortex scene (SZA = 48°). The straight line has 5/3 slope.

vortex scenes. Each subregion consists of 1024×1024 pixels. Spectral slopes fitted separately at large (>0.5 km) and small (<0.5 km) scales are compared. B4 slopes are in all cases steeper than B7 slopes, indicating a less variable radiation field. This is consistent with the expectation that conservative photons transfer between pixels more effectively, thus more effectively reducing the apparent variability of the cloud water field (i.e., as perceived by the radiometer).

Scale breaks of power spectra are linked to processes of radiative smoothing and roughening, whose strength depends on physical cloud characteristics such as thickness, cloud water path, and cloud top variability, so that spectral analysis is a useful tool in cloud radiation studies. Spatial power spectra are also useful guides in the selection of the appropriate cloud optical property retrieval technique (IPA, NIPA, or NDNR; see below) and for evaluating the quality of the retrievals, as discussed in Oreopoulos, Cahalan, et al. (2000) and Oreopoulos, Marshak, et al. (2000). Landsat-7 will continue to provide a rich collection of scenes with different dominant cloud types leading to further improvement of spectral analysis techniques used to detect and interpret 3D effects.

2.2. IPA retrievals and atmospheric radiation measurement (ARM) validation

Despite the already discussed inadequacy of the IPA approximation to provide accurate pixel-level retrievals, it

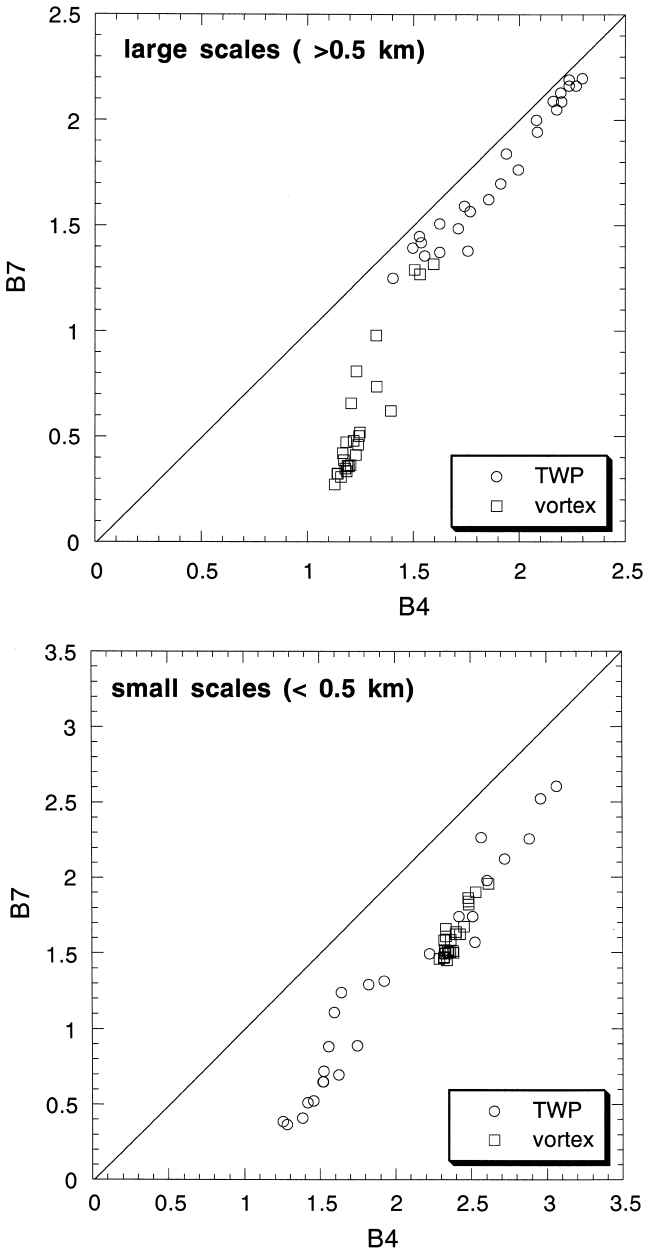

Fig. 3. Comparison between B4 and B7 power spectra log–log slopes as derived from linear least-square fitting. We distinguish between large scales (>0.5 km, top) and small scales (<0.5 km, bottom).

remains a fast, easily implemented, and often adequate tool for obtaining cloud property statistics from satellite measurements. It is not surprising therefore that it has been used for inversion of Landsat-4 and -5 radiances (e.g., Barker, Wielicki, & Parker, 1996; Harshvardhan, Wielicki, & Ginger, 1994; Nakajima, King, Spinhirne, & Radke, 1991). When conditions allow implementation of the IPA (i.e., little shadowing, weak multiple scattering, and large averaging area), Landsat observations are a useful dataset for validating retrievals from coarser resolution radiometers or even surface observations. ETM+ is a particularly valuable validation instrument due to the location of Landsat-7 preceding the Terra platform in the same orbit. For example, in case studies where MODIS retrievals of cloud fraction and properties are flagged uncertain, the ETM+ measurements are a valuable aid. The value of Landsat-7 measurements is enhanced when combined with surface-based atmosphere and cloud measurement programs such as the Department of Energy's ARM Program. In this subsection (split into two parts), we discuss the aspects of IPA cloud retrievals related to the saturation of Landsat visible bands and collocation with surface instruments.

2.2.1. Landsat-7 and cloud saturation

One of the innovations in the design of ETM+ is the ability to operate at two gain settings: high and low. High gain provides the benefit of obtaining strong and well-defined visible signals over vegetation and agricultural surfaces, while low gain is often needed to reduce the amount of saturation over highly reflective surfaces such as desert, ice, and clouds. In the "long-term acquisition plan" (Goward et al., 1999), the default gain settings are high for the solar bands (except the pan band and B4 when the SZA is less that 45°) over most landmasses and over oceans. Depending on illumination conditions, these settings can change over ice, desert, and some other types of surfaces. Moreover, the long-term acquisition plan is designed to fulfill investigators' requests for scene acquisitions at settings they consider optimal for the specific situation. As will be shown below, for studying clouds, it is best to obtain imagery at low gain.

Fig. 4 shows the high and low gain saturation nadir reflectances (corresponding to the maximum ETM+ count of 255) at cosine of SZA $\mu_0 = 0.55$ for all 30 m solar bands. Landsat-5 saturation reflectances are also included for comparison. As can be seen, with the exception of Band 1 (B1), all saturation reflectances at high gain setting are lower than those for Landsat-5. When the gains are set to low, however, the saturation reflectances for ETM+ exceed those for TM.

At what cloud optical thickness does a certain band saturate? In other words, what is the maximum optical thickness that can be retrieved from Landsat reflectances? Unfortunately, there is no unique answer. The absolute amount of solar radiation reaching the cloud and subsequently (partially) reflected towards the detector is obviously a major factor and depends on the SZA. Other factors are atmospheric conditions, droplet size, and surface albedo, but these are usually less important than the 3D structure of the clouds and the sun angle, controlling both the amount of radiation and its 3D spatial distribution. Since observed Landsat reflectances include 3D effects, inverting the maximum reflectance values with plane-parallel theory will not give an accurate estimate of the maximum optical thicknesses that can be retrieved. Still, a relative comparison between Landsat-5 and -7 can be made.

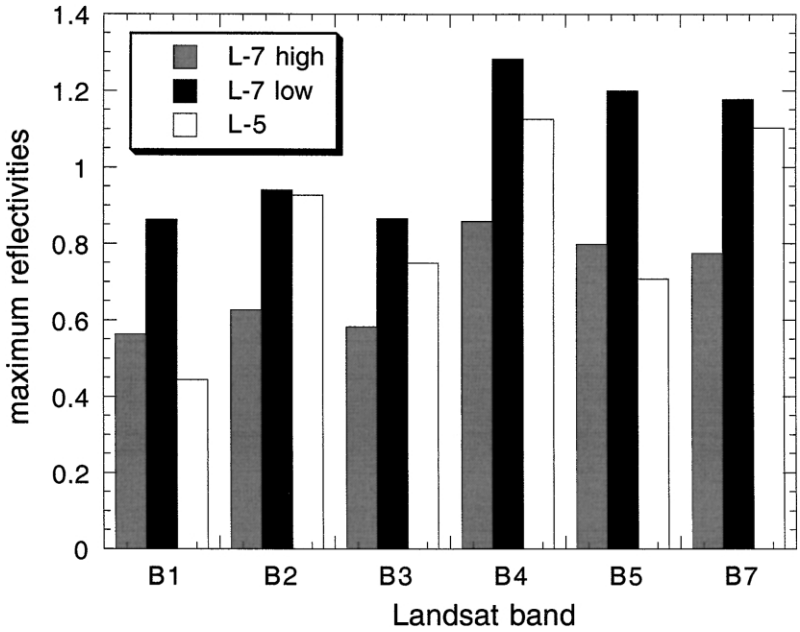

Fig. 4. Maximum (saturation) reflectivities for the six reflective (visible and near-infrared) ETM+ bands at both high and low gain settings. The corresponding TM values have also been included for comparison.

Fig. 5 shows results from such a calculation. We plot the maximum optical thickness that can be retrieved by ETM+ B4 at both gain settings vs. μ_0 and compare to corresponding values for Landsat-5. B4 was chosen because experience with Landsat-5 proved that it did not saturate as often as the other Landsat-5 visible bands. Surface reflectivity was set to 0.2, effective droplet radius to 10 μm, and the weak atmospheric attenuation was only crudely accounted for. (These factors do not significantly affect the results shown here). When a curve reaches 100 (which is the case for all $\mu_0 < 0.5$), saturation is not likely to be a problem under plane-parallel conditions (exact values of maximum optical thickness cannot be given since reflectivity for such thick clouds varies very slowly and retrievals become very uncertain). As can be seen, the retrieval ability of ETM+ greatly improves when the B4 gain is set to low, with problems only at very high sun, while at high gain, limited ability to retrieve should be expected under the same conditions. Things deteriorate for B1–B3, with B2 being the second best choice as indicated by Fig. 4. We emphasize again that these curves correspond to plane-parallel theory and do not address the question of how likely it is to encounter a saturated nadir reflectivity at a certain μ_0, given the change in the amount of incident solar flux. Based on these results, requests for Landsat acquisitions for cloud studies should be made with low gain settings.

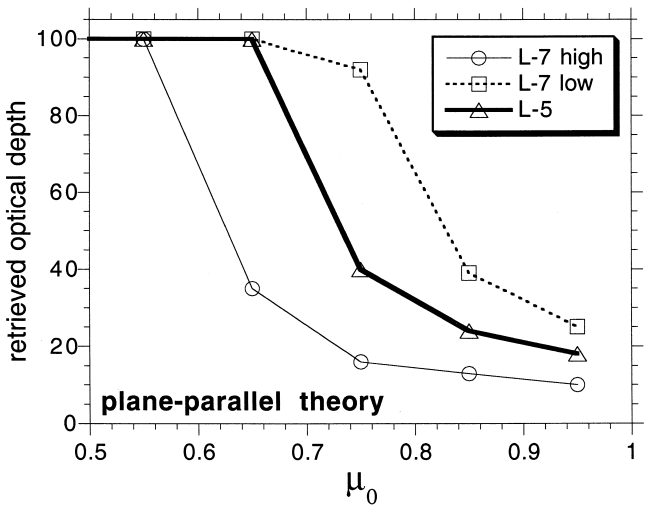

Fig. 5. Optical depth retrieved from plane-parallel theory at high and low gains as a function of the cosine of SZA (μ_0) for maximum (saturation) B4 reflectivities. Retrievals for the corresponding Landsat-5 B4 reflectivities are also shown for comparison. The limit of 100 in optical depth is arbitrary and should be interpreted as an indication that no saturation problems are expected. The value of 100 also applies for all μ_0's not shown.

2.2.2. Comparison with microwave radiometer (MWR) measurements at ARM sites

Another application of Landsat IPA retrievals is validation of surface and other spaceborne retrievals over experiment sites. Using measurements over the Oklahoma ARM site, Oreopoulos, Cahalan, et al. (2000) have shown that useful statistical comparisons between surface and Landsat-5 cloud retrievals can be achieved. Similar results for Landsat-7 are presented in Fig. 6 where the first two moments and histograms of MWR-inferred and ETM+-retrieved liquid water path (LWP) are compared. There is fairly good agreement for both the

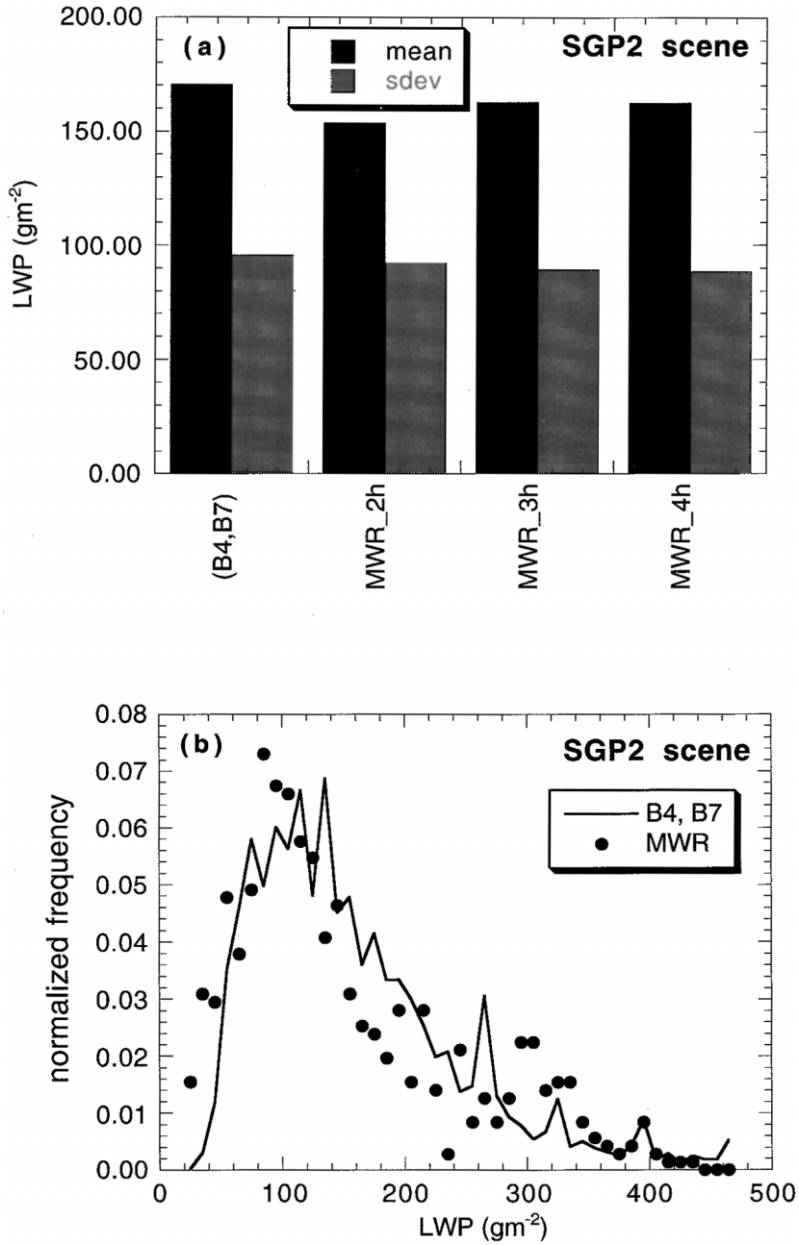

Fig. 6. (a) Means and standard deviations of LWP from Landsat-7 retrievals for the SGP2 scene (see Table 1) and MWR time series at the Oklahoma ARM site centered at various hours around the satellite overpass. (b) Comparison between LWP histograms from the MWR time series for 2 h before and 2 h after the Landsat-7 overpass (dots) and from the Landsat-7 retrievals (solid line). All values below 20 g m^{-2} have been omitted in both plots.

moments and the histogram, given the differences in measurement technique and in spatial and temporal resolution. Landsat measurements are nearly instantaneous, covering an area ~ 180 km^2, whereas the MWR performs (virtually) line measurements over a period of time (various time periods have been used in the moments plot). To obtain the best match, one has to identify in the Landsat scene the exact clouds that have been advected over the MWR while hoping that "frozen turbulence" conditions apply. In this case, we used Landsat retrievals over the entire scene since it is almost overcast and appears relatively uniform.

The above is an example of a procedure that will be repeated routinely with Landsat-7 data, but also MODIS and EO-1 data, while cloud radar (MMCR) will be used as an additional surface probe. The high spatial resolution of ETM+ is helpful in the development of techniques that optimize cross-comparisons of instruments with very different characteristics. Another goal is to use the synthesis of satellite and surface measurements for constructing cloud fields as realistic as possible, which can be used as input to 3D radiative transfer simulations such as those conducted under the aegis of I3RC, the international intercomparison of 3D radiation codes (see http://i3rc.gsfc.nasa.gov).

2.3. NIPA and NDNR retrievals

Landsat-7 measurements are used to develop and improve retrieval techniques that correct for 3D radiative effects present in high-resolution radiometric observations. Two such techniques are NIPA (Marshak, Davis, Cahalan, & Wiscombe, 1997) and NDNR (Oreopoulos, Cahalan, et al., 2000). Both techniques transform the observed imagery affected by radiative smoothing or roughening (or both) to bring it closer to satisfying IPA assumptions. By accomplishing this, retrievals with look-up tables constructed from plane-parallel calculations become more accurate. NIPA removes radiative smoothing, which, as discussed earlier, is more apparent under low SZA conditions, while NDNR removes roughening that occurs primarily at high SZAs. Because both smoothing and roughening occur to some extent under all illumination conditions, our ultimate goal is to develop a method capable of removing both effects simultaneously, e.g., a hybrid NIPA–NDNR method. We believe that Landsat-7 will provide the impetus for expanding and consolidating these techniques and for developing a set of methods that evaluate their performance.

The core of the inverse NIPA transformation is given in Eq. (1) (for details, see Marshak et al., 1998):

$$R_{\mathrm{NIPA}}(\gamma;x) = \int \frac{R_{3\mathrm{D}}(k)}{G(k)} f(\gamma;k)\exp(-ikx)\mathrm{d}k \qquad (1)$$

where $G(k)$ is the Fourier transform of the cloud Green's function, approximated by a γ distribution:

$$G(\alpha,\eta,x) = cx^{\alpha-1}\exp(-x/\eta) \qquad (2)$$

and

$$f(\gamma;k) = \exp(-\gamma^2 k^2) \qquad (3)$$

is a stabilization function to deal with the ill-posed nature of the problem (Eqs. (2) and (3)). In the above equations, R_{NIPA} is the reflectivity obtained after applying the inverse NIPA transformation on the observed or simulated reflectivities that include 3D effects, $R_{3\mathrm{D}}$; x is the location coordinate, α and η are parameters defining the shape of the γ distribution (c is its normalization constant), and γ is a free parameter modulating the stabilization function. The transformation is carried out in Fourier space (hence, the appearance of wavenumber k). The premise of inverse NIPA is that the R_{NIPA} field is a good approximation to the IPA field corresponding to the actual optical depth distribution and is more appropriate for look-up table inversion than $R_{3\mathrm{D}}$, since it is devoid of the smoothing due to net photon horizontal transport.

The main idea of NDNR (Oreopoulos, Cahalan, et al. 2000) is that retrievals using the normalized index

$$\mathrm{NDNR} = \frac{R_{\mathrm{c}} - R_{\mathrm{a}}}{R_{\mathrm{c}} + R_{\mathrm{a}}}, \qquad (4)$$

formed by the reflectivity at a conservative wavelength R_{c} and the reflectivity at an absorbing wavelength R_{a}, behave similarly to IPA retrievals at small SZAs but remove shadowing and side illumination effects at large SZAs. The

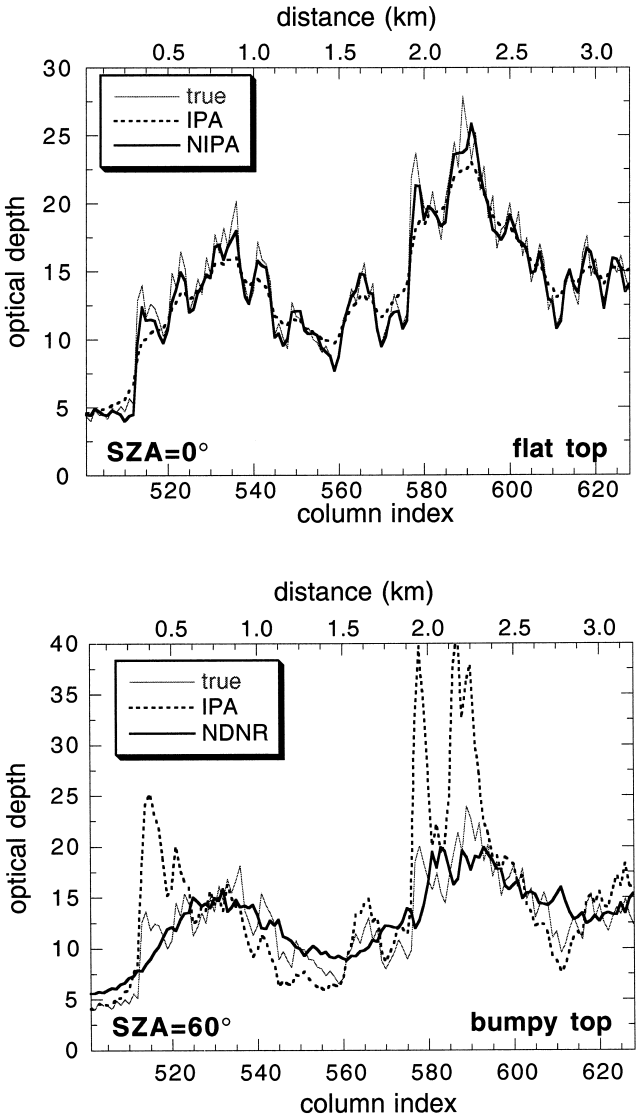

Fig. 7. Comparison of true cloud optical depth with optical depth retrieved using IPA, NIPA (top), and NDNR (bottom) methods from nadir reflectivities generated by radiative transfer from an assumed optical depth distribution. A 128-column segment is shown, taken from a 1024-column optical depth field generated with the bounded cascade model and illuminated with SZA = 0° (top) or SZA = 60° (bottom). For the latter case, AZA azimith angle = 0° (sun shining from left). Column width is 25 m. Surface is assumed black and there are no atmospheric effects. A Henyey-Greenstein phase function with $g = 0.85$ was used in 2×10^8 photon simulations. We show two types of cloud-top variations: flattop cloud (top) and "bumpy" cloud (bottom). Cloud bumps are generated with a fractional Brownian motion model (for a sketch, see Marshak, Wiscombe, Davis, Oreopoulos, & Cahalan, 1999) and are not correlated with optical depth (they also change the optical depth slightly compared to the flat cloud). For both cases, the mean geometrical thickness is 0.3 km, but for the "bumpy" case, cloud geometrical thickness varies from 0.22 to 0.38 km. The NIPA parameters chosen were $\eta = 0.09$, $\alpha = 1.0$, $\gamma = 0.002$.

underlying principle is that these 3D effects are similar for the two wavelengths and are removed when using look-up tables of Eq. (4), thus improving retrievals over those using look-up tables of R_c.

Tests of both NIPA and NDNR have been conducted with radiative simulations, which have the advantage that the "truth" is known in advance: the optical depth field used as input in the radiative transfer model. Results from such tests are shown in Fig. 7 where a segment of an optical depth field from a 1D bounded cascade cloud (Cahalan, Ridgway, Wiscombe, Bell, & Snider, 1994), taken as "truth," is compared to the optical depth retrieved by inverting MC reflectivities, with the upper panel showing IPA vs. NIPA and the lower panel showing IPA vs. NDNR. In the first case of high sun (SZA = 0°), it is noted that IPA retrieves too smooth an optical depth field, while in the second case of low sun

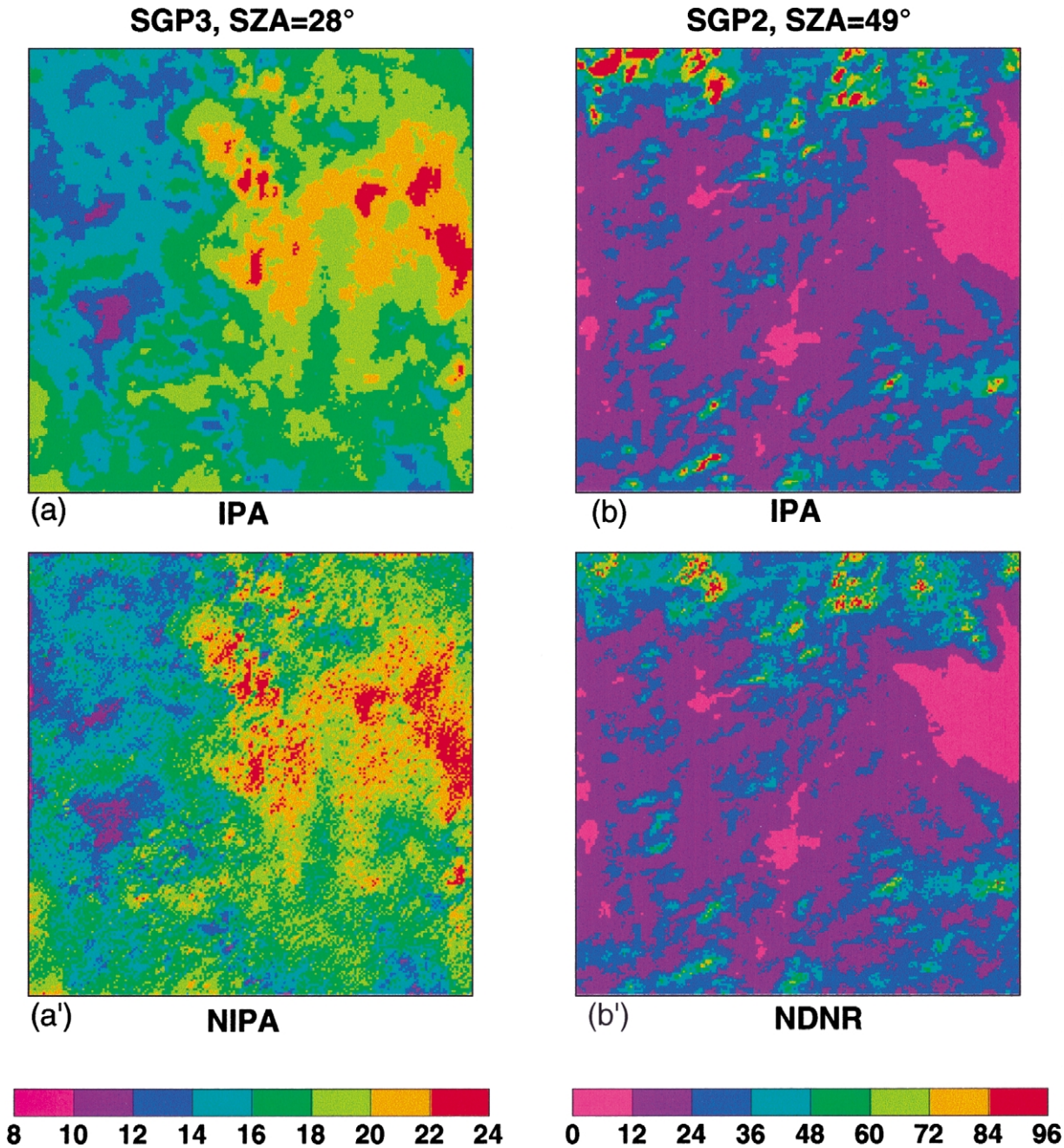

Fig. 8. Optical depth retrievals for a subregion of the SGP3 scene (left) and a subregion of the SGP2 scene (right). (SZA = 28° for SGP3, SZA = 49° for SGP2.) IPA and NIPA retrievals for the SGP3 subregion used look-up table inversion of B4 reflectivities (R4) for effective radius $r_e = 10$ μm; retrievals for the SGP2 subregion used R4 and R7 look-up tables for the IPA case and NDNR=(R4 − R7)/(R4 + R7) and R7 look-up tables for the NDNR case. Atmospheric effects were accounted for using correlated k distributions developed by D. Kratz (personal communication, 2000). Surface albedos for B4 and B7 were set to 0.2 and 0.3, respectively. The parameters for the NIPA case are $\eta = 0.035$, $\alpha = 1.0$, $\gamma = 0.0005$.

(SZA = 60°), an optical depth field that is too rough. In both cases, retrievals are improved.

Fig. 8 shows the result of applying NIPA on a 2D subregion of the "Southern Great Plains", SGP3, scene with the relatively small SZA of 28° and a subregion of the SGP2 scene with a relatively large SZA of 49°(see Table 1). The top panels show IPA retrievals. NIPA can be seen to remove smoothing, and NDNR retrievals can be seen to remove many of the maxima in optical depth caused by the increased side illumination. Though the true optical depth field is unknown, the values retrieved from NIPA and NDNR give wavenumber spectra much closer to the 5/3 straight line of Fig. 2 than do IPA retrievals. (We have verified that spectra from Fig. 8 are similar to those previously published in Oreopoulos, Cahalan, et al., 2000; Oreopoulos, Marshak, et al., 2000 and are optimal when parameters are slightly smaller than in Fig. 8. For brevity, the spectral plots are omitted here.)

Once we have available an extensive database of Landsat-7 cases with different cloud types, these cloud retrieval techniques will be evaluated, with the goal of improving the selection of optimal parameters, quality control, and other implementation details that will facilitate their use in an automated setting. Combined use of simulations and high resolution Landsat-7 radiometry are likely to continue to improve our understanding of 3D radiative processes and our ability to account for 3D radiative effects in cloud retrievals.

3. Aerosol path radiance method

A major Landsat program goal is the long-term monitoring of land surface and biosphere processes on a global scale. However, atmospheric processes often obscure surface reflective properties viewed from satellite. Atmospheric effects include molecular scattering primarily in the visible, water vapor absorption in the near-IR and scattering and absorption by particulates (aerosols and clouds). Since the molecular scattering is well described by Rayleigh scattering theory and Landsat-7 ETM+ bands are selected to minimize water vapor absorption (excluding the panchromatic band at 0.52–0.9 μm), the task of atmospheric correction for Landsat imagery mainly consists of aerosol and cloud adjacency effect corrections.

3.1. Correction for aerosol effects

The correction of Landsat and other high-resolution satellite data for aerosol effects is a challenging task. Unlike selective gaseous absorption, aerosol particles interact with solar radiation over the whole shortwave spectrum. Surface reflection, aerosol scattering, and the interaction between surface and aerosols contribute to radiances observed by ETM+, making it a coupled problem, thus more difficult due to the fact that surface and aerosol properties change spatially and temporally.

A "dark object" approach has been suggested to retrieve aerosol optical thickness and to correct satellite images (Kaufman, Tanre, et al., 1997, Kaufman, Wald, et al., 1997; Liang et al., 1997). The technique uses empirical relations between surface reflectance in the visible bands (in particular, B1 at 0.49 μm and B3 at 0.66 μm) and the mid-IR band (B7 at 2.2 μm; for details, see Kaufman, Wald, et al., 1997). This often works well in tropical regions with large aerosol loading. However, the visible and mid-IR surface reflectance relations change with time and geographic location, giving rise to errors in aerosol optical thickness retrieval and, as a result, errors in atmospheric correction and retrieved surface properties (Wen, Tsay, Cahalan, & Oreopoulos, 1999).

In a study of Landsat-5 TM data, we developed a "path radiance technique" to retrieve aerosol optical thickness over land and to remove the atmospheric effect in surface reflectance estimates (Wen et al., 1999). The physical basis of the technique is that surface reflectances of visible B1 and B3 and the mid-IR B7 are linearly correlated over vegetation and wet soil, as observed by Kaufman, Tanre et al. (1997) and Kaufman, Wald et al. (1997). We showed that this implies a similar correlation in the "apparent" reflectances at the top of the atmosphere, which in turn determines the aerosol path radiance and optical thickness. Below, we summarize the technique. (From here on, we use the term "apparent reflectance" to mean the top-of-the-atmosphere reflectance observed by satellite.)

Away from strong source regions, aerosols tend to be horizontally stratified. For a horizontally homogenous aerosol layer, the apparent reflectance in the visible may be expressed as

$$\alpha_{\mathrm{vis}} = \alpha_{\mathrm{vis}}^{\mathrm{atm}} + T_{\mathrm{vis}}(\mu_0)T_{\mathrm{vis}}(\mu)\rho_{\mathrm{vis}}/(1-\rho_{\mathrm{vis}}R) \tag{5}$$

and in the mid-IR as

$$\alpha_{2.2\ \mu\mathrm{m}} = T_{2.2\ \mu\mathrm{m}}(\mu_0)T_{2.2\ \mu\mathrm{m}}(\mu)\rho_{2.2\ \mu\mathrm{m}} \tag{6}$$

where in Eq. (5), $\alpha_{\mathrm{vis}}{}^{\mathrm{atm}}$ is the path radiance in reflectance units, $T_{\mathrm{vis}}(\mu_0)$ is the transmittance of solar radiation to the surface for cosine of SZA, μ_0, $T_{\mathrm{vis}}(\mu)$ is the transmittance of surface upwelling radiation to the top of the atmosphere for satellite viewing direction μ, ρ_{vis} is the surface reflectance, and R is the diffuse reflectance of the atmosphere in the visible; similar notations are used in Eq. (6) for the mid-IR (Liou, 1980; Wen et al., 1999).

When $\rho_{\mathrm{vis}}R$ is small, which holds for B1 and B3 over wet soil and vegetation, multiple reflection between cloud and surface becomes negligible, so Eq. (5) simplifies to

$$\alpha_{\mathrm{vis}} \approx \alpha_{\mathrm{vis}}^{\mathrm{atm}} + T_{\mathrm{vis}}(\mu_0)T_{\mathrm{vis}}(\mu)\rho_{\mathrm{vis}} \tag{7}$$

Suppose the surface reflectance in the visible and the mid-IR bands are linearly related:

$$\rho_{\mathrm{vis}} = \xi\rho_{2.2\ \mu\mathrm{m}} \tag{8}$$

where ξ = constant. Then, substituting Eq. (8) into Eqs. (6) and (7), the apparent reflectance is

$$\alpha_{\mathrm{vis}} \approx \alpha_{\mathrm{vis}}^{\mathrm{atm}} + \frac{T_{\mathrm{vis}}(\mu_0)T_{\mathrm{vis}}(\mu)}{T_{2.2\ \mu\mathrm{m}}(\mu_0)T_{2.2\ \mu\mathrm{m}}(\mu)}\xi\alpha_{2.2\ \mu\mathrm{m}}. \quad (9)$$

Therefore, the visible and B7 apparent reflectances are linearly correlated if their surface counterparts are linearly correlated and aerosol layers are horizontally homogeneous. Even though the approximation (Eq. (7)) is used to explain the physics leading to Eq. (9), a full radiative transfer calculation indeed demonstrates linear relations between the visible and mid-IR apparent reflectance for a range of aerosol optical thickness when their surface reflectance counterparts are linearly correlated (Wen et al., 1999.)

Extrapolating the visible and mid-IR relation to the intercept where the apparent reflectance of mid-IR is zero determines the path radiance of the visible bands. Here, we assume that aerosol does not affect the mid-IR, so that *zero apparent reflectance in B7 implies zero surface reflectance*. The path radiance in the visible bands is determined from the apparent reflectance of this imaginary surface of zero reflectance. From the path radiance, the aerosol optical thickness is determined, and the aerosol effect may then be removed to determine the visible surface reflectance.

The path radiance method is a generalization of the statistical method applied operationally to MODIS aerosol retrievals (Kaufman, Tanre, et al., 1997; Kaufman, Wald, et al., 1997). It is an improvement over the MODIS approach because it does not assume a universal correlation but derives a correlation from each scene individually. This more accurate method is necessary when aerosol loading is small. More importantly, the path radiance approach is the first attempt to decouple atmospheric effects from surface contributions in satellite remote sensing of aerosol optical thickness and surface reflectance.

3.2. Clear-sky correction near clouds

Research on atmospheric correction has focused so far on clear-sky conditions, well separated from any clouds. In a clear atmosphere, solar radiative transfer may be accurately described by the plane-parallel assumption (Stamnes, Tsay, Wiscombe, & Jayaweera, 1988; Tsay, Stamnes, & Jayaweera, 1990). However, the atmosphere often contains many clouds. Even when cloud cover is low, satellite images in many geographic locations often reveal widely scattered fair-weather cumulus clouds. Clouds make the surrounding atmosphere appear extremely inhomogeneous, so that radiances exiting clear patches become difficult to interpret. With the 16-day repeat cycle of Landsat-7, to exclude all scenes with scattered cumulus would substantially reduce the harvest of useful surface measurements. In order to make better use of high-resolution images of the surface, we need to understand how clouds affect radiation in nearby clear regions.

In the following, we use a partially cloudy Landsat-7 scene to demonstrate the path radiance technique, first in an entirely cloud-free subscene and then in a partially cloudy subscene, to exhibit the impact of clouds on aerosol and surface retrievals. The scene was acquired on June 4, 1999 over the Oklahoma SGP site of the DoE/ARM program, with SZA of 24°. Fig. 9 shows a color composite, with RGB = B7, B4, B2. Clouds appear white due to the relatively weak wavelength dependence in the visible reflectivity of clouds, while surface vegetation and soil show larger wavelength dependence. The left portion of the image is covered with cumulus clouds. A cumulus congestus cloud appears on the right edge of the image. Large portions of the upper right and lower middle of the image are cloud free. The clear region contained in the black rectangle at the upper right is reproduced in a blowup in the lower right corner, and the cloudy region contained in the rectangle at the upper left appears in a blowup in the lower left corner. Both regions have the same size of 30×30 km.

The scatterplots in Fig. 10 show pixel apparent reflectances for the visible (B1 at 0.49 μm and B3 at 0.66 μm) and mid-IR (B7 at 2.2 μm). Red scatter points are from the clear region on the right of Fig. 9, and blue scatter points are from the cloudy region on the left. For the clear region, the visible and mid-IR apparent reflectances demonstrate good linear relations. A straight line least-square fit through the lower envelope of the red scatter points has a zero mid-IR reflectance intercept of 0.09 and 0.025 for B1 and B3, respectively, and these intercepts give the aerosol path radiance in those two bands.

The scattered blue points in Fig. 10, from the cloudy region of Fig. 9, fall into two categories or branches. The upper branch lies near the line of equal visible and mid-IR reflectance, indicating that it comes from the cloudy pixels, which have weaker wavelength dependence. The lower branch comes from the clear patches of the cloudy scene and also exhibits a good linear correlation between visible and mid-IR reflectances, similar to that in the cloud-free region. However, this lower clear branch of the blue scatter points appears shifted up by $\sim 0.01-0.02$ in both B1 and B3. Since we expect the aerosol path radiance itself to be approximately uniform over the 180 km Landsat swath, the shifts of the clear-sky branch seen in Fig. 10, from the "all clear" red points to the "near cloud" blue points, must be primarily due to increased surface illumination from visible light that has been scattered from cloud sides and interacted with aerosols.

This interpretation of Fig. 10 is aided by a simplified simulation of the effect of an isolated cloud on nadir radiance, computed using a 3D MC radiative transfer scheme (Marchuk et al., 1980; Marshak et al., 1995). The isolated cloud is taken to be 1 km thick and 2 km on a side, with vertical optical thickness 20 in visible and mid-IR. The cloud is placed in the center of a 25.6×25.6 km domain, with grid cells of 200 m. The phase function is that

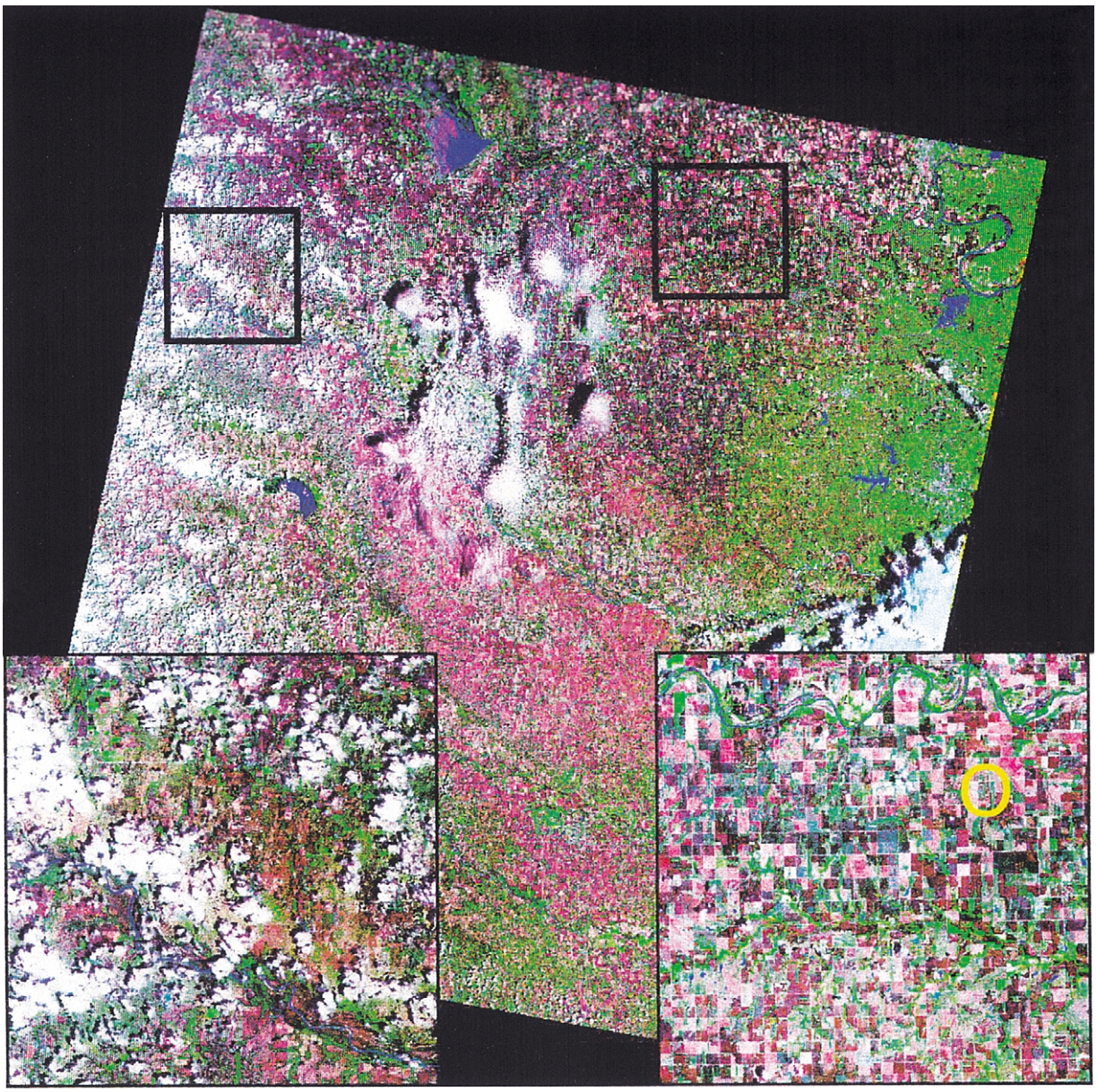

Fig. 9. Landsat-7 ETM+ image acquired on June 4, 1999 with B7, B4, and B2 displayed as red, green, and blue. SZA is 24°. The zoomed images in the lower left (cloudy) and lower right (clear) correspond to the regions in square boxes in the upper left and upper right of the image, respectively. The circle in the lower right zoomed image encloses the DoE/ARM Central Facility at the Oklahoma site.

of a modified γ cloud droplet distribution, with effective radius of 6 μm and effective variance of 0.111 (Deirmendjian, 1969; Hansen & Travis, 1974). A continental aerosol model (d'Almeida, Koepke, & Shettle, 1991; Shettle & Fenn, 1979) is used to compute the aerosol-scattering phase function and single-scattering albedo. The surface has a Lambertian reflectance of 0.05, the SZA is 30°, and the azimuth angle is 0° (sun shining from the left along the x-axis). For clarity, we plot the difference of apparent reflectance between cloudy atmosphere and clear atmosphere in the principal plane (x–z) of the Sun, and the perpendicular plane, through the center of the cloud. The simulation is performed for wavelengths 0.5 (B1) and 2.2 μm (B7). The aerosol optical thickness is taken to be 0.2 at 0.5 μm and 0.0 at 2.2 μm.

The apparent visible reflectance in the presence of the cloud, minus that for no cloud, for a 1 km cloud base, is shown in Fig. 11. At the grid point adjacent to the cloud on the sunward side of the principal plane (i.e., left of the cloud in Fig. 11a), the nadir reflectance is enhanced by 0.015. Away from the cloud, the enhancement decreases and reaches positive asymptotic values of less than 0.005 in 2–3 km. On the antisun side of the principal plane, to the right of the cloud in Fig. 11a, the negative difference in grid points near the cloud indicates the presence of a distinct cloud shadow. Away from this shadow, the

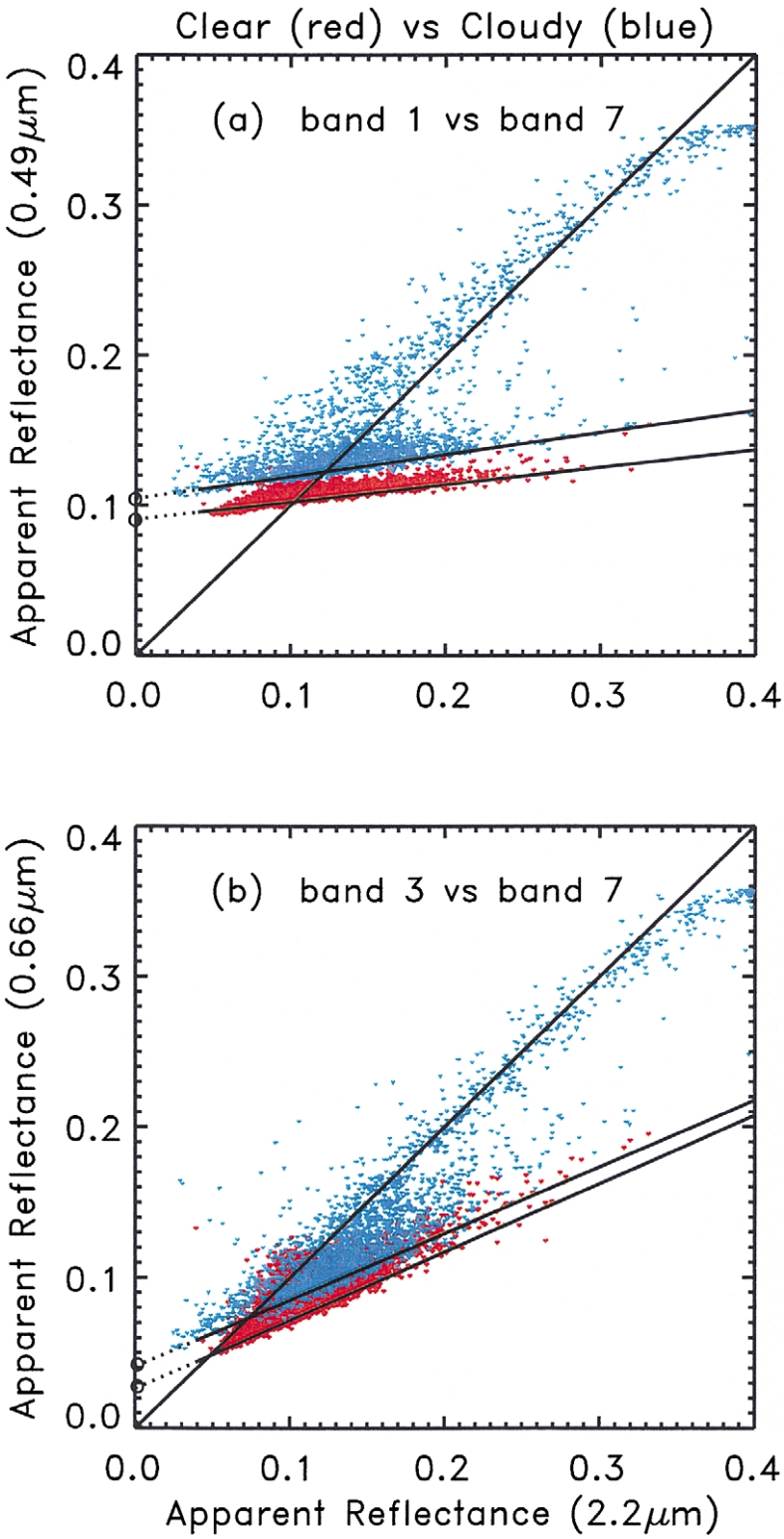

Fig. 10. The apparent reflectance relations between (a) B1 and B7 and (b) B3 and B7 for the clear subscene (red scatter points) and the cloudy subscene (blue scatter points) shown in the zooms of Fig. 9.

enhancement is less than 0.005 similar to that on the sunward side with same distance away from the cloud. In the plane perpendicular to the principal plane, the enhancement to either side of the cloud is symmetrical, with a maximum value about 0.01 at the adjacent grid points, decreasing to positive asymptotic values less than 0.005 in a distance about 2–3 km away, to either side of the cloud. Surprisingly, in both planes, there remains a small but

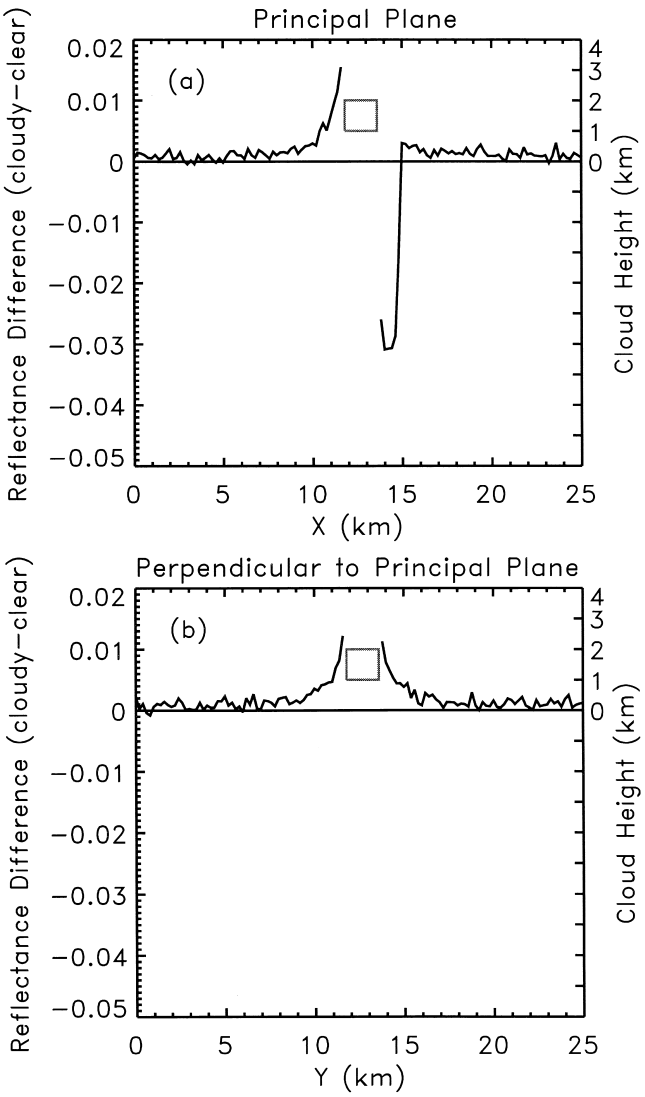

Fig. 11. 3D MC simulation of the impact of an isolated cloud on ETM+ B1 reflectance, showing the difference of nadir reflectance between a scene with cloud and one with no cloud, both with aerosol optical thickness of 0.2. Cloud base is at 1 km and top at 2 km, with optical depth of 20 and horizontal dimensions 2 × 2 km. The horizontal position is indicated by the box at 12.8 km. Differences are presented in (a) for the principal plane and (b) the plane perpendicular to it.

significant bias (i.e., exceeding MC noise), even 10 km on either side of the cloud!

Nadir reflectance differences from the same simulation, except for the B7 band, are presented in Fig. 12. The pattern of enhancement of the nadir reflectance near the cloud is similar to that in the visible bands, but cloud effects are smaller in both planes, reaching zero at a distance of about 3 km. Simulations performed with clouds placed in various vertical locations and with different vertical extent produced similar results. Generally, cloud adjacency effects are larger at visible than at mid-IR wavelengths, but most importantly, in the visible, the enhancement is still significant even 2–3 km from the cloud while it virtually disappears over a similar distance in the mid-IR. Note that, unlike in the visible, at larger distances, no bias is evident in Fig. 12. This shows that the bias in Fig. 11 is due to the interaction between cloud and aerosol. (The relatively smaller MC noise in Fig. 12 is due to lack of aerosol scattering in the mid-IR.)

An actual Landsat ETM+ cloud image is, of course, much more complex than the cloud in this simple simulation. Unfortunately, simulating a realistic fair weather cumulus cloud scene, of even small area, is computationally expensive. The observed enhancement of visible reflectance is evidently larger than that due to the isolated cuboidal cloud. Particularly, in cloud shadows, the model results show a large decrease of apparent reflectance that does not appear in observations. This indicates that surrounding clouds have significant contribution to the observed radiance. The inhomogeneity of cloud optical properties can also have large impact on the observed enhancement. At the cloud edges, the optical path is expected to be small. The thinner

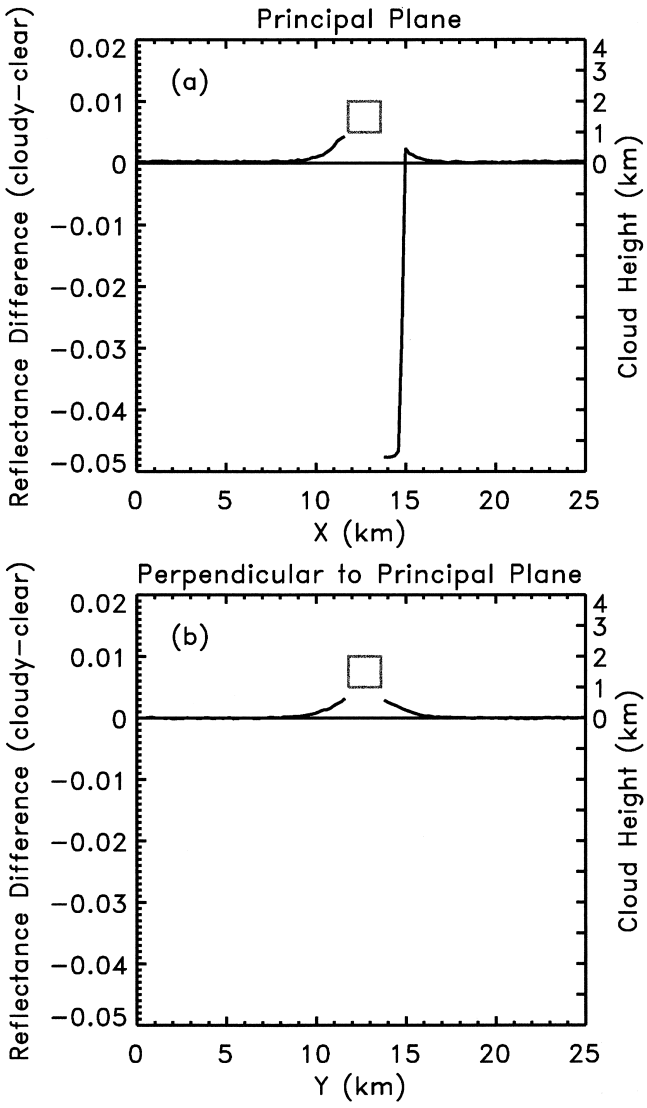

Fig. 12. Same as in Fig. 3 but for ETM+ B7. Atmospheric effects are ignored.

cloud edges not only allow more direct solar radiation passing through but also generate more diffuse radiation than optically dense clouds, leading to increased illumination of the aerosol layer and the surface. The results presented above provide a physical understanding for the shift in the visible and mid-IR apparent reflectance for clear patches between scattered cloud, such as those encountered in the lower left subscene of Fig. 9 and the corresponding scatter plots in Fig. 10. More extensive MC simulations are needed to explain other features, such as the impact of cloud shadows on Fig. 10.

The cloudy subscene for which the blue points of Fig. 10 are plotted is about 30×30 km in size. The distance from a clear pixel to a nearby cloudy pixel ranges from 30 m (1 pixel) at cloud edge to about 2 km. Since the cloud side-scattering effect is generally larger at visible bands than at mid-IR, due to longer mean-free-path and greater interaction with aerosols, the enhancement of surface illumination due to nearby cloud is also expected to be greater in the visible than in mid-IR. This phenomenon is more evident in clear regions about 2–3 km away from clouds where cloud side-scattering effects are zero for mid-IR. In a scattered cumulus cloud region such as the one shown in Fig. 9, each individual cloud acts as a source of surface radiation due to side scattering. In such a region, the enhancement of visible nadir radiance in the clear gaps likely exceeds that occurring adjacent to the isolated cloud of Fig. 11. For the mid-IR band where the aerosol-scattering effect is negligible, cloud adjacency effects are limited to distances significantly smaller than 2–3 km.

In summary, a significant enhancement of visible illumination in clear patches surrounding clouds was found due to multiple scattering between clouds and aerosols. As a result, path radiance has a significant positive bias, as does retrieved aerosol optical thickness, producing a positive bias in surface reflectance. Fig. 10 shows that this affects only the intercept, not the slope, suggesting subtraction of a constant visible radiance. Further research with Landsat-7 data is currently underway to study this phenomenon in realistic situations.

4. Conclusions

With the help of cloud, aerosol, and surface retrievals from several Landsat-7 scenes, this paper shows that:

- Cloud, aerosol, and surface retrievals are linked and influenced by 3D cloud radiative effects.
- 3D scattering effects lead to overestimates of aerosol loading and consequent overestimates of surface reflectance.
- Aerosol and surface biases depend on mean distance to cloud.
- Landsat-7's radiometric and spatial resolution are effective in dealing with joint atmosphere-surface retrievals.
- Landsat-7's B4 and B7, set at low gain, are preferred for cloud retrieval.
- B7 is useful in retrieving low aerosol amounts in the visible B1 and B3.

Two recently introduced methods of cloud retrieval are described: NIPA (Marshak et al., 1998) and NDNR (Oreopoulos, Cahalan, et al., 2000). These approximately account for cloud radiative smoothing and cloud shadowing, respectively. Also, the recently introduced "path radiance method" of aerosol retrieval and clear-sky correction (Wen et al., 1999) is reviewed and contrasted to the method of universal statistical correlations (Kaufman, Tanre, et al., 1997; Kaufman, Wald, et al., 1997) now being used operationally for MODIS.

The essential interdependence of cloud and clear-sky retrievals was shown by applying the path radiance method to clear pixels in a region of scattered cumulus in a Landsat scene containing the Oklahoma ARM site. A clear increase in the *apparent path radiance* is seen, which produces significant errors in derived surface reflectance when the cloud effect is ignored. We indicated how the cloud effect may be removable from the aerosol path radiance by subtracting a constant visible radiance and used a simple MC simulation to illustrate this. This hypothesis needs further testing.

Clearly, much more analysis and simulation will be needed before reliable guidelines can be established to account for cloud adjacency effects. The main conclusion here is that, in typical clear-sky situations containing both aerosol and scattered cumulus, accurate surface properties may be retrieved only when proper account is taken of the interdependent contributions of surface, aerosol, and clouds on Landsat-7 radiances.

Acknowledgments

The authors wish to thank Pat Scaramuzza of USGS for providing the data for Fig. 1, W. Wiscombe for discussions on cloud fractal structure and retrieval, and Y. Kaufman for discussions about the MODIS aerosol retrieval algorithm. This research was funded by the NASA Landsat Program Office, as part of the Landsat-7 Science Team under NASA grant 1996-MTE-00116, the NASA Radiation Sciences Program under NASA RTOP 6224257, and by the Department of Energy Atmospheric Radiation Measurement (ARM) program under grants DE-AI02-97ER62369 and DE-AI02-00ER62939.

References

Barker, H. W., Wielicki, B. A., & Parker, L. (1996). A parameterization for computing grid-averaged solar fluxes for inhomogeneous marine boundary layer clouds: part II. Validation using satellite data. *Journal of the Atmospheric Sciences*, *53*, 2304–2316.

Batchelor, G. K. (1967). *An introduction to fluid dynamics*. Cambridge, UK: Cambridge Univ. Press (615 pp.).

Cahalan, R. F. (1994). Bounded cascade clouds: albedo and effective thickness. *Nonlinear Proceedings in Geophysics*, *1*, 156–167.

Cahalan, R. F., Ridgway, W., Wiscombe, W. J., Bell, T. L., & Snider, J. B. (1994). The albedo of fractal stratocumulus clouds. *Journal of the Atmospheric Sciences*, *51*, 2434–2455.

Cahalan, R. F., Ridgway, W., Wiscombe, W. J., Harshvardhan, W. J., & Gollmer, S. (1994). Independent pixel and Monte Carlo estimates of stratocumulus albedo. *Journal of the Atmospheric Sciences*, *51*, 3776–3790.

Cahalan, R. F., Silberstein, D., & Snider, J. B. (1995). Liquid water path and plane-parallel albedo bias during ASTEX. *Journal of the Atmospheric Sciences*, *52*, 3002–3012.

Cahalan, R. F., & Snider, J. B. (1989). Marine stratocumulus structure. *Remote Sensing of Environment*, *28*, 95–107.

d'Almeida, G. A., Koepke, P., & Shettle, E. P. (1991). *Atmospheric aerosols: global climatology and radiative characteristics*. Hampton, LA: Deepak (561 pp.).

Davis, A., Marshak, A., Cahalan, R. F., & Wiscombe, W. J. (1997). The Landsat scale break in stratocumulus as a three-dimensional radiative transfer effect, implications for cloud remote sensing. *Journal of the Atmospheric Sciences*, *54*, 241–260.

DeFelice, T. P., Meyer, D. J., Xian, G., & Cahalan, R. F. (2000). Landsat 7 reveals more than just surface features in remote areas of the globe. *Bulletin of the American Meteorological Society*, *81*, 1047–1049 (includes cover photo).

Deirmendjian, D. (1969). *Electromagnetic scattering on spherical polydispersions*. New York, NY: Elsevier (292 pp.).

Goward, S. N., Haskett, J., Williams, D., Arvidson, T., Gasch, J., Lonigro, M., Reeley, M., Irons, J., Dubayah, R., Turner, S., Campana, K., & Bindschadler, R. (1999). Enhanced Landsat capturing all the Earth's land areas. *EOS Transactions American Geophysical Union*, *80*, 289–293.

Hansen, J. E., & Travis, L. D. (1974). Light scattering in planetary atmospheres. *Space Science Reviews*, *16*, 527–610.

Harshvardhan, Wielicki, B. A., & Ginger, K. M. (1994). The interpretation of remotely sensed cloud properties from a model parameterization perspective. *Journal of Climate*, *7*, 1987–1998.

Kaufman, Y. J., Tanre, D., Gordon, H. R., Nakajima, T., Lenoble, J., Frouin, R., Grassl, H., Herman, B. M., King, M. D., & Teillet, P. M. (1997). Passive remote sensing of tropospheric aerosol and atmospheric correction for the aerosol effect. *Journal of Geophysical Research*, *102*, 16815–16830.

Kaufman, Y. J., Wald, A., Remer, L., Gao, B.-C., Li, R.-R., & Flynn, L. (1997). The MODIS 2.1 mm channel correlation with visible reflectance for use in remote sensing of aerosol. *IEEE Transactions on Geoscience and Remote Sensing*, *35*, 1286–1298.

Liang, S., Fallah-Adl, H., Kalluri, S., JáJá, J., Kaufman, J., & Townshend, J. R. G. (1997). An operational atmospheric correction algorithm for Landsat Thematic Mapper imagery over the land. *Journal of Geophysical Research*, *102*, 17173–17186.

Liou, K.-N. (1980). *An introduction to atmospheric radiation*. Orlando, FL: Academic Press (392 pp.).

Marchuk, G., Mikhailov, G., Nazaraliev, M., Darbinjan, R., Kargin, B., & Elepov, B. (1980). *The Monte Carlo methods in atmospheric optics*. New York, NY: Springer-Verlag (208 pp.).

Marshak, A., Davis, A., Cahalan, R. F., & Wiscombe, W. J. (1998). Nonlocal independent pixel approximation: direct and inverse problems. *IEEE Transactions on Geoscience and Remote Sensing*, *36*, 192–205.

Marshak, A., Davis, A., Wiscombe, W. J., & Cahalan, R. F. (1995). Radiative smoothing in fractal clouds. *Journal of Geophysical Research*, *100*, 26247–26261.

Marshak, A., Wiscombe, W. J., Davis, A., Oreopoulos, L., & Cahalan, R. F. (1999). On the removal of the effect of horizontal fluxes in two-aircraft measurements of cloud absorption. *Quarterly Journal of the Royal Meteorological Society*, *125*, 2153–2170.

Nakajima, T., King, M. D., Spinhirne, J. D., & Radke, L. F. (1991). Determination of the optical thickness and effective particle radius of clouds from reflected solar radiation measurements: part II. Marine stratocumulus observations. *Journal of the Atmospheric Sciences*, *48*, 728–750.

Oreopoulos, L., Cahalan, R. F., Marshak, A., & Wen, G. (2000). A new normalized difference cloud retrieval technique applied to Landsat radiances over the Oklahoma ARM site. *Journal of Applied Meteorology*, *39*, 2305–2321.

Oreopoulos, L., Marshak, A., Cahalan, R. F., & Wen, G. (2000). Cloud effects evidenced in Landsat spatial power spectra and autocorrelation functions. *Journal of Geophysical Research*, *105*, 14777–14788.

Shettle, E. P., & Fenn, R. W. (1979). Models for the aerosols of the lower atmosphere and the effects of humidity variations on their optical properties. *AFGL-TR-79-0214, Environmental Research Paper No. 675*, NTIS ADA 085951, (94 pp.).

Stamnes, K., Tsay, S.-C., Wiscombe, W. J., & Jayaweera, K. (1988). Numerically stable algorithm for discrete-ordinate-method radiative transfer in multiple scattering and emitting layered media. *Applied Optics*, *27*, 2502–2509.

Tsay, S.-C., Stamnes, K., & Jayaweera, K. (1990). Radiative transfer in stratified atmospheres: development and verification of a unified model. *Journal of Quantitative Spectroscopy & Radiative Transfer*, *43*, 133–148.

Wen, G., Tsay, S.-C., Cahalan, R. F., & Oreopoulos, L. (1999). Path radiance technique for retrieving aerosol optical thickness over land. *Journal of Geophysical Research*, *104*, 31321–31332.